Spectrum of Engineering Sciences
ISSN (e) 3007-3138 (p) 3007-312X Volume 3, Issue 12, 2025

TO STUDY ELECTRONIC AND OPTICAL PROPERTIES OF $QZrO_3$ [Q = Ba, Ca, Sr] BY ALL ELECTRON METHOD

Kulsoom Fatima[1], Umme Kalsoom[2], Farrukh Sohail[3], Saeed Hassan[*4], Mubeen Shahid[5]

[1,2,3]*Department of Physics, University of Lahore, Sargodha Campus, Sargodha, Punjab, Pakistan*
[*4,5]*Department of Mechanical Engineering, University of Management and Technology, Sialkot Campus, Sialkot, Punjab, Pakistan*

[1]kulsoom05fatima@gmail.com, [2]ummek8926@gmail.com , [3]farrukhsohail72@gmail.com, [*4]saeed.hassan@skt.umt.edu.pk,[5]mub99n@outlook.com

DOI: https://doi.org/10.5281/zenodo.18265314

Keywords

Article History
Received: 03 November 2025
Accepted: 17 December 2025
Published: 31 December 2025

Corresponding Author: *
Saeed Hassan

Abstract

The Wien2k code's accurate all-electron FP-LAPW [full potential linearized augmented plane wave] approach with GGA (Generalized Gradient Approximation) is used to investigate the optical and electrical properties of the alkaline earth metal zirconate perovskites QZrO3 (Q = Ba, Ca, Sr). It is determined that the theoretically computed lattice constants correlate well with the empirically measured values. All of the compounds listed are known to be indirect gap barriers. For these compounds, optical constant dispersion such as the fictive and actual elements of dipole functions, absorption values, refractive indexes, reflectivity, and absorption coefficients have also been computed. These polycrystalline structures may find application in electronic, thermal coating materials, and optical systems operating in the UV-visible region of the electromagnetic spectrum due to their high absorption qualities.

INTRODUCTION

Gustav Rose, a Russian mineralogist discovered the perovskite structure in 1839. He found $CaTiO_3$, later called a mineral by C.L.A. Von Perovski, the Russian mineralogist. *Lemanov, V. V., et al. (1999)* stated that the acquisition of $CaTiO_3$ as orthorhombic crystals has been observed [1]. *Mitchell, R. H. (2002)* stated that the broadest equation is ABX_3, with a metal cation A and B and an anion X. Oxygen forms the structure of ABO_3 that applies to this research often are non-metallic anions. The perovskite structure can be adapted and misused to adjust its primary subtleties and current characteristics [2]. *Woodward, P. M. (1997)* stated that perovskite has major variations like monoclinic, tetragonal, rhombohedral, and triclinic, but the cubical structure is the ideal undistorted design [3]. *Feng, L. M., et al. (2008)* stated that *Figure* 1. (a) shows the design, which is represented by a cubic cell unit. There are 12 cubooctahedral anions surrounding the unit cell centre, which contains enormous cations such as Na^{1+}, K^{2+}, Sr^{2+}, Ba^{2+}, Y^{3+}. Small cations are addressed in (b). Ga^{3+}, Zr^{4+}, In^{3+}, $Sn^{4+,}$ Ti^{4+}, Mn^{4+}, Nb^{5+} on unit cell edges surrounded by six octahedral co-ordinate anions (c). Two B-site cations and four A-site cations enable the binding of (X) to non-metallic anions, such as O^{-2}, Cl^{-1} and F^{-1}. Oxygen is the most prominent molecule in position X however it might be any member of the halogen family [4].

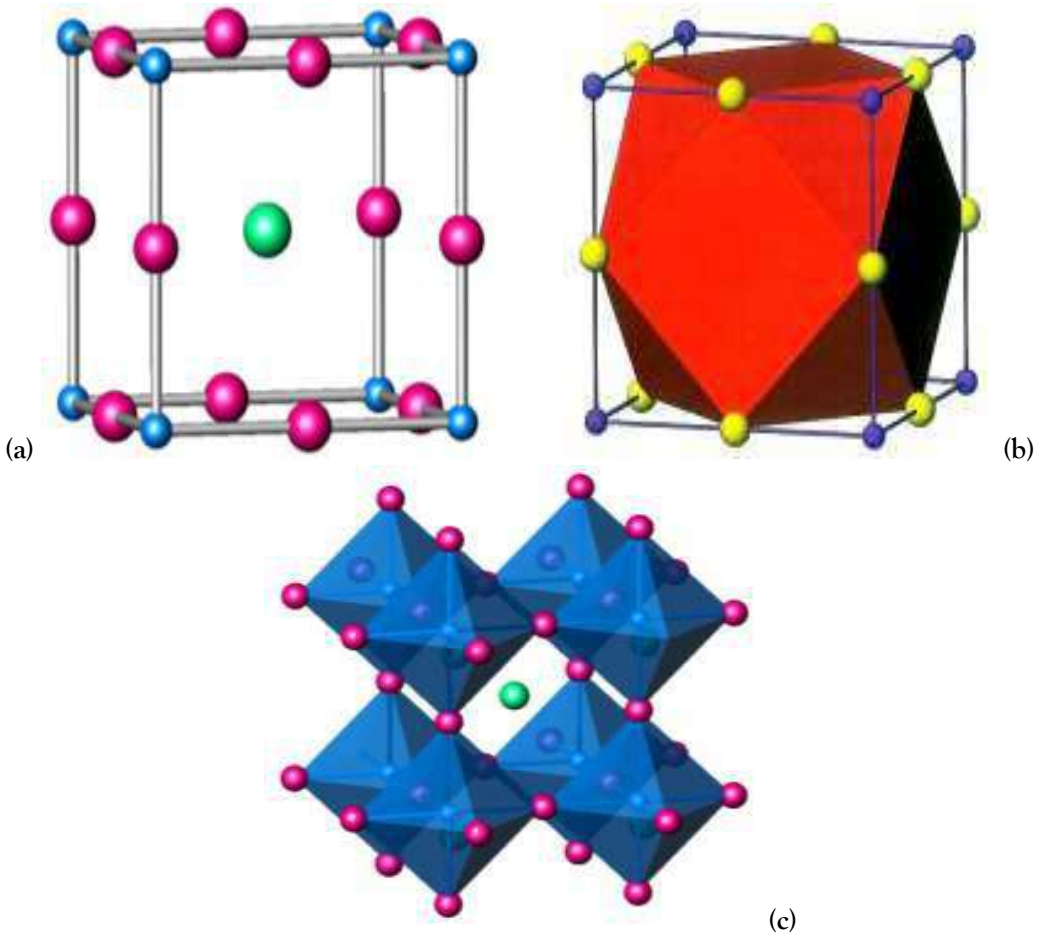

Figure 1: (a) Simple perovskite structure (b) AX_{12} is the unit cell for the cubo-octahedral polyhedron (c) Cation A is enclosed in an octahedral 8-X anion perovskite projection.

Kong, L. B., et al. (2008) stated that ferroelectric ceramics are regarded as one of the leading utilitarian material classes. The Curie temperature (TC) enables them to exhibit uncompromising polarity at a certain temperature [5]. *Haertling, G. H. (1999)* stated that the discovery of ferroelectrics in polycrystalline barium titanate in 1921 researchers have been pondering and utilizing $BaTiO_3$ [6].

Alotaibi, A. (2017) stated that $BaTiO_3$ (BT) is one of the most widely utilized ferroelectric materials. It is justified by its high relative permittivity (dielectric consistency) which increases with temperature and reaches its highest temperature level at TC (130°C) and subsequently decreases at expanding temperatures, as required by Curie-Weiss law [7]. *Burke, J. E. et al. (1957)* stated that there are crystal structure transitions from tetragonal to cubic. It is common for BT to be doped with uncommon earth metals (such as La^{3+}, Y^{3+} or Nd^{3+}) to produce the n type of semi-conductive material. Increases in temperature above TC result in large changes in specific resistivity [8].

Wu, T. B. et al. (1990) stated that in the dielectric structure, BT can be doped with particles such as Sr^{+2} or Pb^{+2} to occupy the Ba site, or Hf^{+4} and Sn^{+4} to occupy the Ti^{+4} site, while the position of TC is determined by ionic radius contrasts [9]. *Issa, M. A. A. (1992)* stated that if the BT semi-conducting structure is doped with the above-mentioned particles, changes in PTCR characteristics must also occur among other

things [10]. *Hamamoto, K. et al. (2003)* stated that PTCR enigma explained by Heywang and Jonker model can be linked to the occurrence of an anticipated grain limit deterioration due to interface acceptor states (g_b) [11]. *Jonker, G. H. (1967)* stated that the potential barrier tallness is equivalent to the relative permittivity. Since its different properties in the DfT industry and also in the manufacturing industry perovskites are vigorously investigated [12].

Fortunately, the ABX_3 natural inorganic semiconductor perovskites have been growing amazingly from advanced. They have lower objects than ABO_3 oxide perovskites, as shown in Table 1.1. Especially in the clear light zone the $CH_3NH_3PbI_3$ perovskites are immediate bandgap halves which show excellent retention. Its bandgap is 1.5 eV and its coefficient of absorption reaches the remarkable locality with 10^5 cm^{-1}.

Table 1.1: Particularity or theoretical bandgap of perovskite materials and experimental bandgaps.

Perovskites	Theoretical bandgap (eV)	Experimental bandgap (V)
$BiFeO_3$	1.9-2.7	1.9-2.7
$PbTiO_3$	2.87	3.2
$SrTiO_3$	3.57	3.75
γ-$CsSnI_3$	1.3±0.1	1.3
$CH_3NH_3PbI_3$	1.3-1.61	1.50-1.61
$CH_3NH_3PbBr_3$	2.3	2.32
$CH_3NH_3PbI_{3-x}Cl_x$	-	1.55-1.64
$HC(NH_2)_2PbI_3$	1.47	1.47

Brown, A. et al. (2011) stated that in the winter of these days, PM2.5 is being contaminated in Beijing China by the overabundance of oil derivatives. The petroleum products are another important issue and their stores cannot be used especially consistently. As we probably know, the production of fossil coal, petroleum and oil takes a long time to shape the power that can be used, when the plant or creature material rolls into the Earth's hull. Non-renewable energy sources in this way are currently not inexhaustible [13].

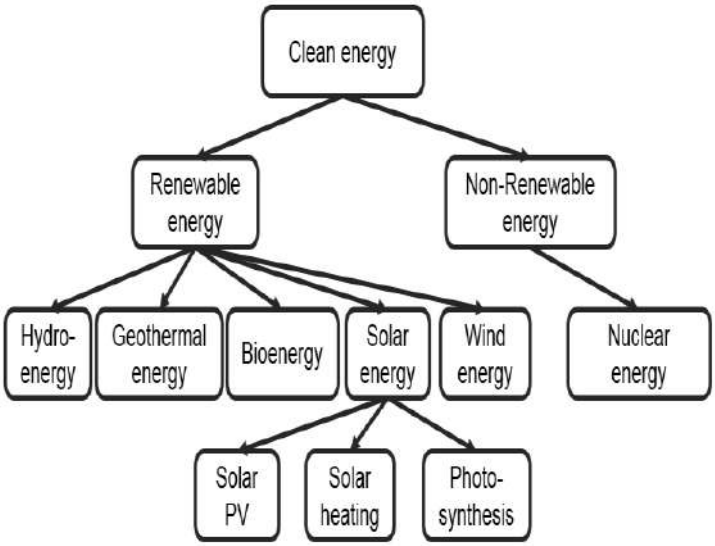

Figure 2: Different types of renewable energies.

Green, M. A. (2015) stated that during the new year's, numerous new sun powered cells were created. As shown in Figure 3 these sun-based cells are arranged into three ages, depending on their assembly interaction and progress. [14].

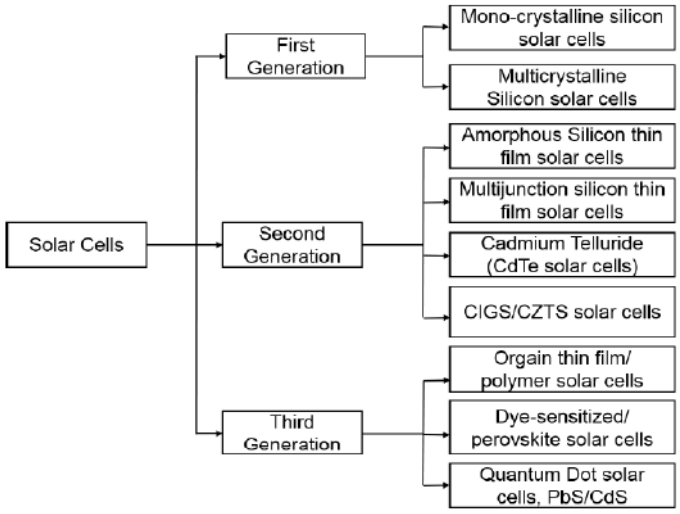

Figure 3: Classification of various solar cell technology.

Liu, D. et al. (2014) stated that the efficiency of the force change was 20% in 2015 as shown in Figure 4 its improvement is much faster than the other cells based on sunlight. In addition, they had various benefits, in particular the reduced expense, in step-up to high efficiency [15].

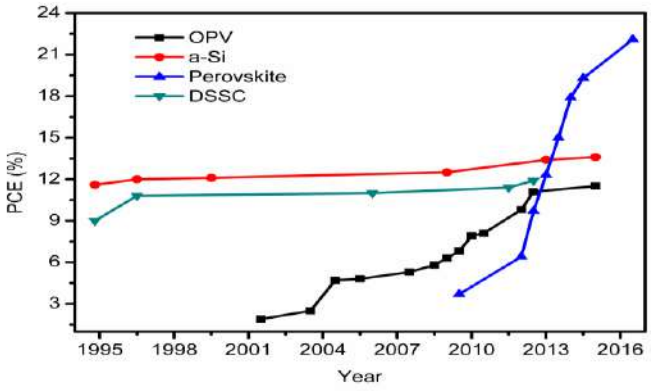

Figure 4: Different types of solar cells' power conversion efficiency over the last two decades.

Cursively, low-temperature arrangements have been made for the ABX_3 and other perovskites based on halide. The basic technique for planning halide perovskite material were shown in Figure 5.

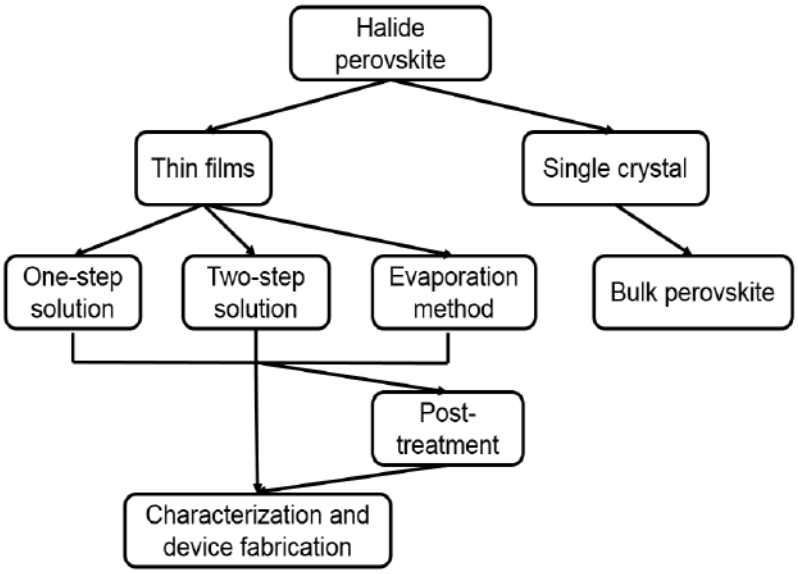

Figure 5: Typical procedure to prepare $CH_3NH_3PbI_3$ perovskite.

Kim, H. S. et al. (2012) stated that in this strategy, Pb $(CH_3COOH)_2 \cdot 3H_2O$ and CH_3NH_3I stoichiometric proportion was disintegrated into the fluid HI arrangement and then warmed up and mixed up. [16]. *Im, J. H. et al. (2014)* stated that the two-venture technique was developed by Nam-Gyu Park et. al. to make ready, peripherally, small films [17].

Figure 7 outline the fundamental techniques of this strategy, which retained the PbI_2 files in the mesoporous TiO_2 layers at the beginning of the process and then stacked the CH_3NH_3I array to react with PbI_2 films and twists covered by perovskite layers.

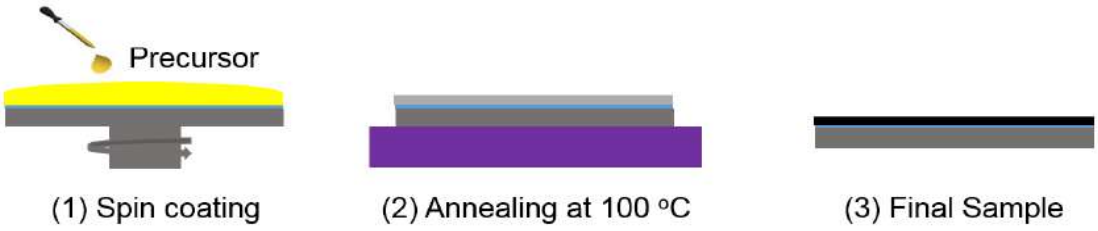

Figure 6: Typical procedures of one-step preparation of $CH_3NH_3PbI_3$ perovskite.

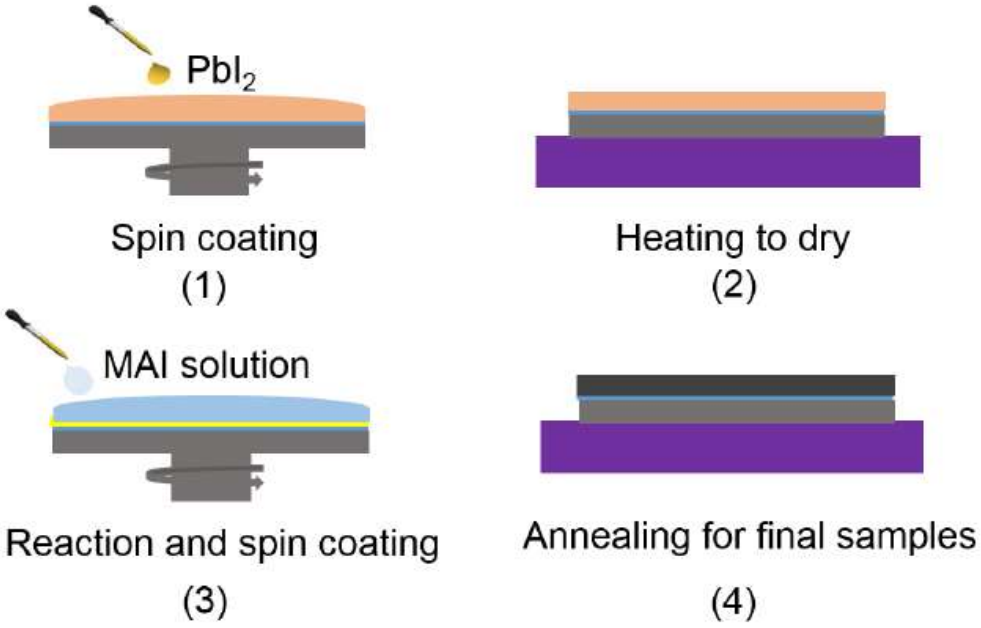

Figure 7: Typical procedures of two-step preparation of $CH_3NH_3PbI_3$ perovskite.

Pazos-Outón, L. M. et al. (2016) stated that Figure 8 outlined the normal engineering of the planar organized perovskite sunlight-based cells. Typically, these types of sun-oriented cells were managed by an adventure strategy in which $PbCl_2$ & CH_3NH_3I mixing arrangements were covered and tempered in a minimum layer. They are easier to produce than mesoporous organized perovskites with sunlight-based sunlight cells, but they have largely hysteresis during the I-V portrait [18].

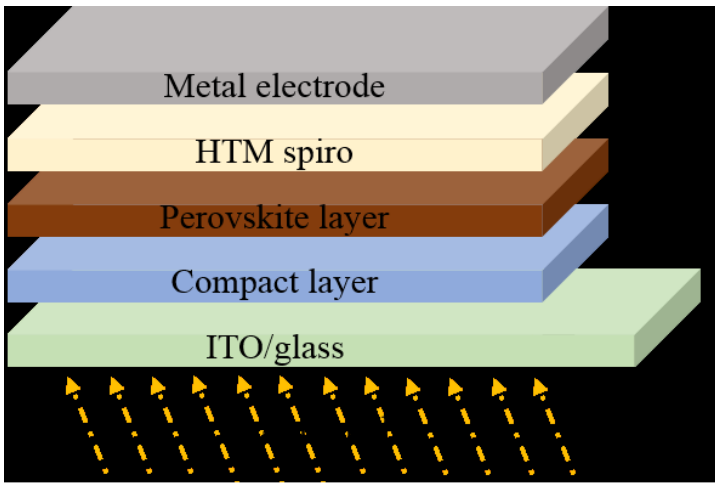

Figure 8: Solar cells with planar halide perovskite structures.

Edri, E. et al. (2014) stated that there is no doubt that perovskite cells that are orientated toward the sun will be potent solar cells. His work guidance was evaluated from sun-oriented cells, sharpened by color [19].

The energy contour appears in Figure 9 and can be presented as a working guideline for perovskite sun-based cells. The photons were assimilated and the electron-opening sets were created at the point when the episode light were applied. They were transported to the conduction belt, and their apertures raced to get to the valence band.

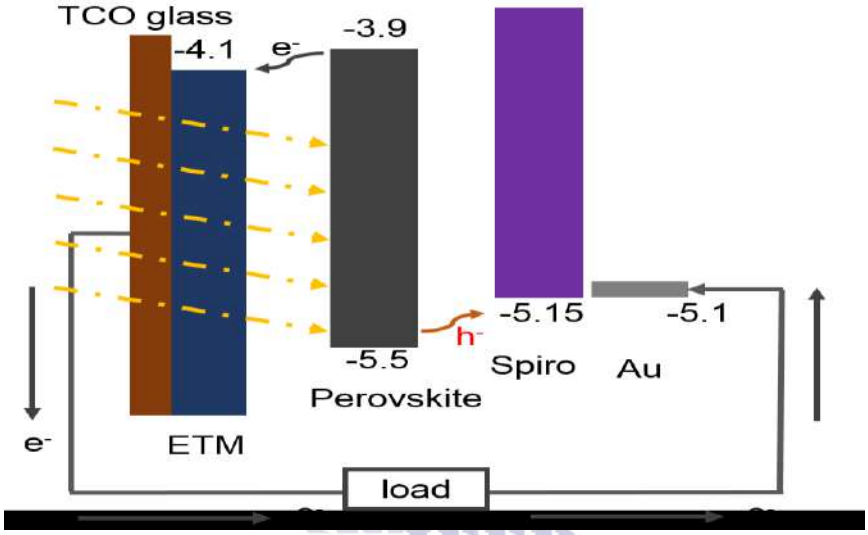

Figure 9: Typical halide perovskite solar cells: energy level diagram and operating mechanism.

However, for perovskite sun-oriented cells, there are still many difficulties. Initially, hysteresis and stability are addressed by the sun-based halide perovskite cells. The nature of perovskite movies, such as crystallization, grain sizing, inclusion and interfaces is accepted as a strong basis. Well, sun-oriented cells are seen as benefiting from crystallization, massive seed, and full inclusion. Second, the sunlight-based halide perovskite cells deal with the problem of plumb contamination, as there is some plumbing in the perovskite layer. Lead contamination is a difficult question that can lead to the natural environment catastrophe. The development of lead-free or plumbing materials is critical to overcoming this problem.

2.LITERATURE REVIEW

Using the GGA-PBE approximation used in the HSE06 formalism within the framework of DFT, N M Ravindra et al. (2021) investigated cubic alkaline-earth metal zirconate perovskites. The strong ionic conductivity of zirconate perovskites is widely recognized. The structural, elastic, electrical, and optical properties of zirconate perovskites are first investigated [20]. Using density functional theory (DFT) and the CASTEP code with Perdew-Burke-Ernzerhof, M. Ramzan et al. (2020) investigated the phase transition, bandgap engineering, and optical response for optical devices of magnesium doped CaZrO3 perovskite.-PBE-GGA, or Generalized Gradient Approximations [21]. Using the (FP-LAPW) approximation as used by WIEN2K software within the context of DFT, S. Dhabi et al. (2020) investigated the new environmentally friendly free of lead zirconate perovskites doped with chalcogens for solar cells [22]. Using the (GGA-PB) approximation within the framework of DFT, Riaz Ahmed et al. (2019) investigated the structural stability of SrZrO3 perovskite and the enhancement of electrical and optical

characteristics by Ca and Ba doping for optoelectronic applications [23].

Muhammad Rizwan et al. (2019) used the GGA approximation in the context of DFT to investigate the impact of magnesium doping on the band gap and optical characteristics of SrZrO3 perovskite. Using the concepts of TDOS and PDOS, the impacts and, subsequently, the optical characteristics of Mg-doping on electronic structures have been fully investigated and characterized [24].

Using the GGA approximation inside the DFT framework, Saad Tariq et al. (2015) investigated pressure-dependent analysis on the optical characteristics of cubic perovskite SrZrO3. Here, optical characteristics of strontium zirconate at various pressures (0, 40, 100, 250, and 350) are given [25]. I. Zeba et al. (2020) used the (PBE-GGA) approximation within the framework of DFT to investigate the impact of anomalous behavior of Be doping on structural stability, bandgap, and optical characteristics in comparison with Mg doped BaZrO3 perovskite [26]. D. M. Hoat et al. (2018) used the (FP-LAPW) approximation, which is implemented in the WIEN2k package within the context of DFT, to study the structural, electrical, and optical properties of perovskites CaZrO3 and CaHfO3 in cubic phase. Because it produces a very precise and stable band gap, the modified Becke-Johnson exchange potential (mBJ) for Tran Blaha is also utilized in electrical and optical simulations [27]. Using Ultrasoft pseudopotentials (USP) and the Generalized Gradient Approximation (GGA-PBE) functional proposed by Perdew, Burke, and Ernzerhof inside the DFT framework, M. Uzma et al. (2020) investigated the role of Zn in modifying the electrical and optical characteristics of SrZrO3 [28]. Using Ultra-soft pseudo-potential (USP), which is included into the Cambridge Serial Total Energy Package (CASTEP) within the DFT framework, S. Aleena et al. (2020) investigated computational understanding of the electrical and optical properties of Cd-doped BaZrO3 [29]. O. Tahiri et al. (2018) used DFT calculations with GGA approximation as implemented in the ABINIT package to examine the structural, electrical, and optical properties of Ba1-xCaxTiO3 and Ba1-xSrxTiO3 (x = 0.4, 0.6). The computed structures show indirect band gaps at M sites with low energy dispersion in a highly symmetrical orientation based on its optimal cell design for solid solutions [30].

Seema Kumari Meena et al. (2019) used the DFT method WC1LYP under the LCAO approximation to investigate Compton spectroscopy and electronic structure for tetragonal barium titanate. It is demonstrated that LCAO-WC1LYP provides stronger support for the experimental data indicating hybrid potential for increased use in BaTiO3 electrical structure prediction [31]. Abdullah Chik et al. (2020) used the first principles approach within density functional theory (DFT) as implemented in Quantum Espresso (QE) with the plane wave pseudo prospective function to study the electrical characteristics of calcium and zirconium co-doped BaTiO3. By doping Ca and Zr, BaTiO3, which has an energy band gap of 3.4 eV in the experimental investigation, can increase its piezoelectricity at sites A and B. Electronic characteristics such band structure, total density of states (TDOS), and partial density of states (PDOS) have an impact on BaTiO3 ca and Zr doping [32].

3.DENSITY FUNCTIONAL THEORY

3.1MATHEMATICAL-TOOLS

3.1.1 Functionals

Rodríguez, J. I. et al. (2009) stated that function takes a number as input and outputs a number. One number is said to be planned to be followed by a second number, etc. a function accepts an input from another function and returns a number as its output [33].

$$y(x) = x^2 \rightarrow y(x = 2) = 4. \quad (3.1)$$

Functional: $F[y(x)] = \int_0^1 y(x)dx \rightarrow F[y = x^2] = \frac{1}{3}$. (3.2)

3.1.2 Functional Differentiation

The energy functionality of DFT should be limited and separation of functions should therefore be an important idea. Think of a variable y factor. When you move from one point to another $(y_0 + \delta y)$, the change in function is:

$$dF = F(y_0 + \delta y) - F(y_0) = F'(y)|_{y0}dy. \quad (3.3)$$

At that point y_n think about a circumstance with various factors. The derivative is defined as the partial derivative:

$$dF = \frac{\partial F}{\partial y_1}\Big|_{y0} dy_1 + \frac{\partial F}{\partial y_2}\Big|_{y0} dy_2 + \cdots \quad (3.4)$$

Martin, R. M. et al. (2020) stated that this aspect explains a functional derivative, but it is not a way of calculating it. However, the modification of the left side can being implicitly calculated by this function.

$$dF = \mathrm{F}[y + \delta y] - \mathrm{F}[y]. \quad (3.5)$$

When the two articulated are achieved the functional alternation and compare it to Eq. (3.6) the differential is determined as:

$$\frac{\delta T_{TF}}{\delta n(r)} = \frac{5}{3} C_F n^{\frac{2}{3}}. \quad (3.6)$$

3.2 THE SCHRONDINGER EQUATION

The laws of quantum mechanics depict the characteristics of matter at the nanoscale. The non-relativistic Schrodinger equation (in nuclear units) administers roughly the conduct of particles and electrons:

$$i\frac{\partial}{\partial t}\,\Psi(\mathrm{r}, t) = \hat{H}\Psi(\mathrm{r}, t). \quad (3.7)$$

In this paper, the second one, called the time-independent Schrodinger Equation (TISE) is used as the strategy known as Density Function Theory, which aims to discover the ground state wave function of a framework. A Hamiltonian with the accompanying structure defines the partnership within a particle arrangement.

$$\hat{H} = -\frac{1}{2}\sum_i^N {\nabla_i}^2 - \frac{1}{2m_A}\sum_A^M \nabla^2{}_A - \sum_i^N \sum_A^M \frac{Z_A}{r_{iA}} + \sum_i^N \sum_{j>i}^N \frac{1}{r_{ij}} + \sum_i^M \sum_{B>A}^M \frac{Z_A Z_B}{R_{AB}}. \quad (3.8)$$

3.3 HARTREE-FOCK

As the state vector $|\psi\rangle$ is multidimensional and multi-electron in nature, utilizing the principle of variation to locate the ground presents a fundamental challenge$|\psi\rangle$. The Hartree-Fock technology's rule strategy is to improve its wave function to make the structure more manageable. For electron-electron collaborations, this uses a medium field portrayal. The Hamiltonian is initially placed in a discrete group in a single and numerous electron terms.

$$\hat{H} = \sum_i h(i) + \sum_{i<j} v(i,j) + v_{NN}. \quad (3.9)$$

$$h(i) = -\frac{\nabla_i^2}{2} - \sum_A \frac{Z_A}{r_{iA}}. \quad (3.10)$$

Without electronic coupling, it is only viable $\sum_i h(i)$, due to single-electron wave functions, to isolate the confounded multi-body state vector.

$$\Psi(r_1 \ldots r_N) = \phi_{i(r_1)}\phi_{j(r_2)} \ldots \phi_k(r_N). \quad (3.11)$$

3.4 BASIS-SETS

The single-electron wave function should be extended for a premise in order to address the single-particle conditions of the Kohn-Sham system. This transforms the arrangement of the whole differential Schrodinger individual particle conditions in a computationally processable framework conditions.

3.4.1 Atomic Orbitals

Sets of nuclear orbital premises offer a fundamental approach to DFT requirements. They are usually received from Schrodinger's responses for a reclusive particle. The spiral structure provides structural elements.

$$R(r) = e^{-r/na_0} r^l L_n. \quad (3.12)$$

3.4.2 Plane Waves

If plane waves are directly mixed, then Kohn-Sham wave functions can likewise be treated such as.

$$\psi_{n,k} = \frac{1}{\Omega} \sum_G c_{G,n,k} e^{iG.r}. \quad (3.13)$$

For various reasons, plane waves were a triumph. They're not unilaterally dependent on the type of frame or iota within. It is possible to traverse between space and k-space via rapid Fourier shifts, making a variety of activities more faster. They also allow the powers to be figured out directly.

3.4.3 Periodicity

It is clear to imitate a confined framework with few iotas. But a massive solid material that would require significant amounts of particulate matter is often required to regenerate.

Nevertheless, a unit-cell of strong cannot be attempted to reassemble and at times reassemble all three spatial measurements. Surfaces can also be mimicked by leaving in one measurement a vacuum hole. An unlimited setup of disengaged frameworks is essentially reconstructed by leaving three measures of vacuum holes. Just as intermittent limits have some computational advantages, they also enable the recast of solids and surfaces. The Bloch hypothesis can be applied in the context where an occasional framework is discussed. This shows that the Schrodinger condition's functions.

$$\psi_{n,k} = \mathcal{U}_{n,k} e^{ik.r}. \quad (3.14)$$

Where $\mathcal{U}_{nk}$ has the cross-sectional periodical. These are the features of an intermittent wave condition. Bloch $\mathcal{U}_{nk}$ is referred to as grid time. A Fourier set of terms, which represent the various cross section vectors, is frequently expanded in these lines as in all intermittent functions. This is because G is the equivalent of plane waves moving forward with their wave vectors.

$$\psi_{n,k} = \frac{1}{\Omega} \sum_G \tilde{\mathcal{U}}_{G,n,k} e^{iG.r}. \quad (3.15)$$

Obviously, there are unlimited numbers of equal cross-sectional vectors with unlimited grid. Bloch's steeper slope results in less substantial upper recurrence parts of this plane wave development. Thus, the development can be reduced at a particular cut-off to a decent estimate. Note that this truncation is necessary and controlled by the measurement of computation accessible handling force and memory. Only parts are included in these lines.

$$|k + G|^2 \frac{h^2}{2m_e} < E_{Cut}. \quad (3.16)$$

The result of the cut off is a wave work that is less exact and a frame that has more vitality. If the figure's ends are affected by truncation, union frameworks should be evaluated. Introduced into Bloch hypothesis articulation of the development for the intermittent Bloch work:

$$\psi_{n,k} = \frac{1}{\Omega} \sum_G c_{G,n,k} e^{iG.r}. \quad (3.17)$$

This frame represents a straight combination of waves in planes. In the first work of a wave that spread the ridiculous space of the occasionally cross-section only one of the intermittent cells became wave work

limited. The wave works should however be determined at an interminable number of k-focuses. It can be prevented by forcing limited conditions for Born von Karmen.

$$\psi(r + N_i a_i) = \psi(r). \quad (3.18)$$

Furthermore, utilizing Bloch's hypothesis.

$$\psi(r + N_i a_i) = e^{(iN_i k_i a_i)}\psi(r)\,. \quad (3.19)$$

The only k values that are valid are those that estimate the exponential function $2n\pi$.

$$k_i = \frac{Integer_i}{N_i} g_i. \quad (3.20)$$

Thereafter there is an indefinable arrangement of unlimited concentrations close to each other when the quantity of $N_i$cells is infinite. On the other hand, the Bloch Wave's arrangements are just interesting from a cross-sectional perspective.

3.4.4 Pseudo-potentials

Coulomb's potential is exceptionally high in the vicinity of an atomic nucleus. If you want to balance this, you'll need a lot of kinetic energy from the wave function and a lot of Fourier components. This difficulty is avoided by using a pseudo-potential.

As a result of their great concentration around the nucleus, the core electrons play little or no influence in the bonding of an atom. The valence electrons are the only ones involved in the bond. In any system, it is a good idea to distribute the electrons in the core in the same way as they would be in an isolated atom. To put it another way, harmonics are solutions multiplied by spherical Schrodinger radial equation. An approximation treatment of the interaction between core electrons and valence electrons, known as pseudo potential, is used instead.

This interaction can be treated using the augmented wave projection method. However, the pseudo-potential approach is the first to be discussed in this regard. Pseudo-potential has a number of benefits. Due to the fact that Kohn-Sham Eigenstates have fewer autonomous data and matrix elements than other Eigenstates, it reduces the number of electrons that need to be calculated.

4.RESULTS AND DISCUSSIONS

4.1 Structure of unit cell

$BaZrO_3$ crystallizes in the cubic space group Pm3m with the lattice parameters: a = 4.256 Å, b = 4.256 Å and c = 4.256 Å with the conventional angle $\alpha = \beta = \gamma = 90^{\circ}$.

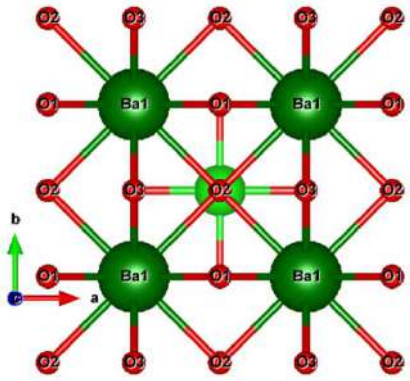

Figure 10: (a) Unit cell of $BaZrO_3$.

$CaZrO_3$ crystallizes in the orthorhombic space group Pnma with the lattice parameters: a = 5.638 Å, b = 5.833 Å and c = 8.107 Å with the conventional angle $\alpha = \beta = \gamma = 90^{\circ}$.

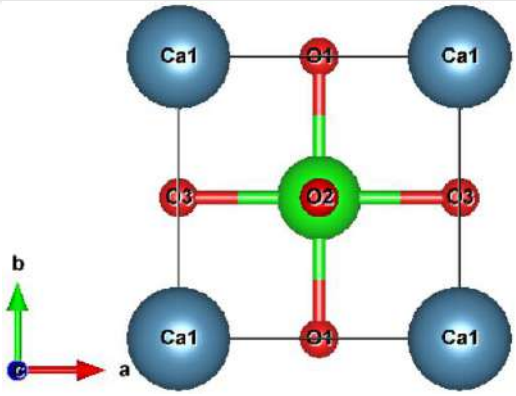

Figure 10: (b) Unit cell of $CaZrO_3$.

$SrZrO_3$ crystallizes in the orthorhombic space group Pnma with the lattice parameters: a = 5.847 Å, b = 5.912 Å and c = 8.298 Å. with the conventional angle $\alpha = \beta = \gamma = 90^{\circ}$.

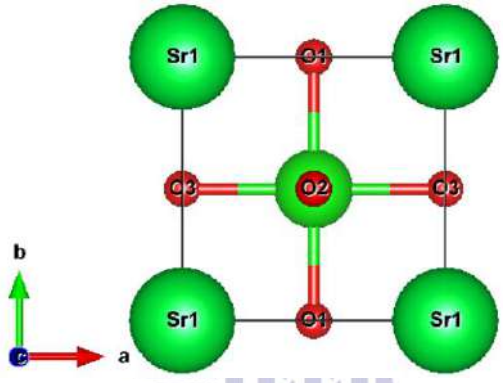

Figure 10: (c) Unit cell of $SrZrO_3$.

4.2 Band Structure

GGA method is used to calculate the band structure of $BaZrO_3$, $CaZrO_3$ and $SrZrO_3$ as indicated in Figure 11, 12 and 13 respectively. Since this approximation provide us with more clear results. The electronic and optical properties of the said material were calculated using same approximation for the sake of batter results.

By taking Fermi level at 0 eV, band structure was plotted from -5.0 eV to 5.0 eV. Also, valence band is from -5 eV to 0 eV and conduction band from 0 eV to 5 eV. We have noticed from band structure that all of these materials are insulators in nature with indirect band gap of for $BaZrO_3$ is 3.8 eV, for $CaZrO_3$ is 3.3 eV and for $SrZrO_3$ is 3.9 eV respectively Since CBM and VBM does not lie on same symmetry lines, that's why the band gap is indirect. Such materials show weak optical excitation. These materials require a phonon in addition to photon and electron for the conduction. But indirect band gap materials (e.g. crystalline Si) are used to make photovoltaic cell. So, this material can also be used in optoelectronic devices.

Calculated band structures (along highly symmetric directions $R \rightarrow \Gamma \rightarrow X \rightarrow M \rightarrow \Gamma$ in brillouin zone) for same spin by using GGA approximation are displayed in Figure, 11,12 and 13.

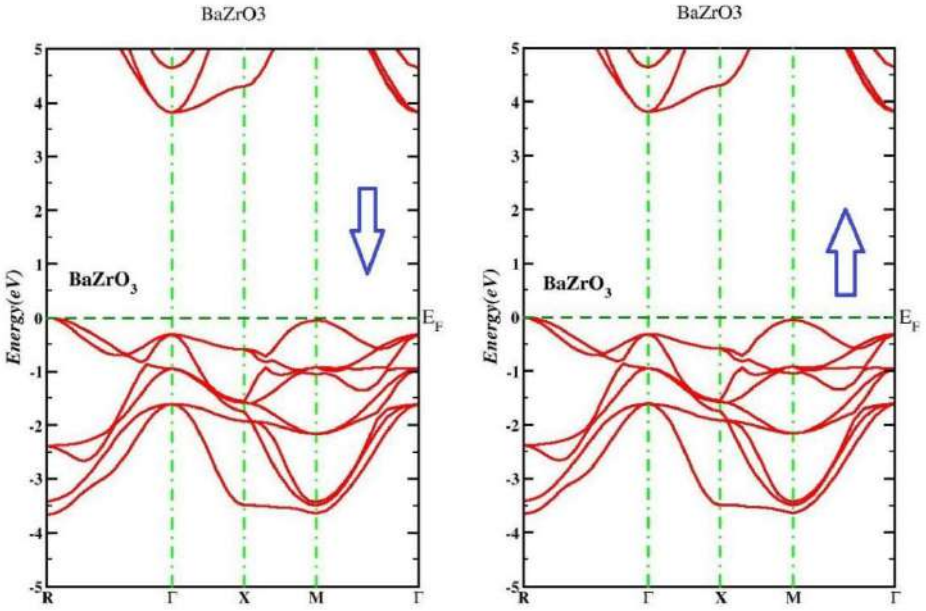

(a) (b)

Figure 11: (a) $BaZrO_3$ spin down and (b) $BaZrO_3$ spin up.

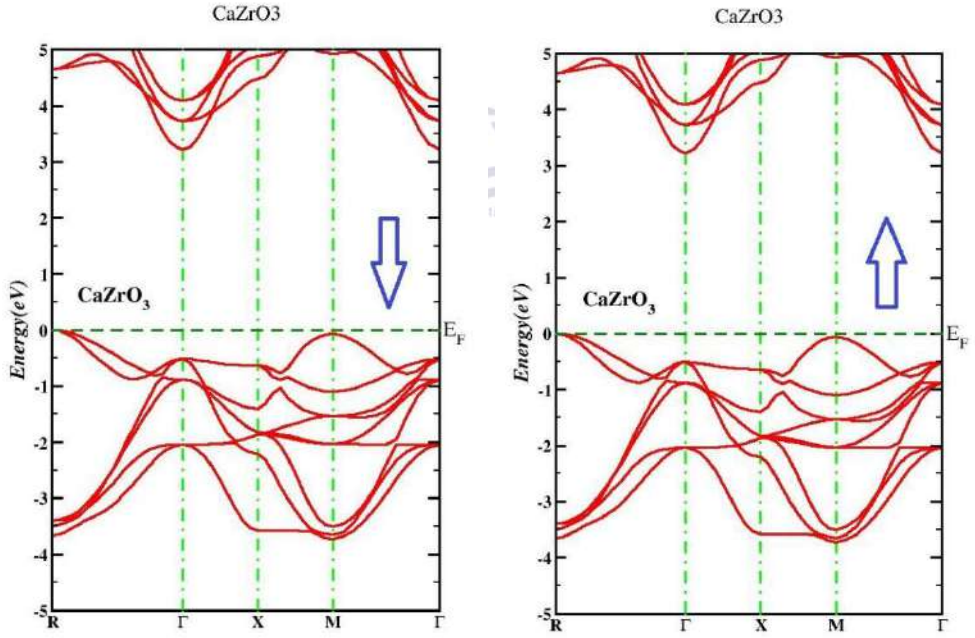

(c) (d)

Figure 12: (c) $CaZrO_3$ spin down and (d) $CaZrO_3$ spin up.

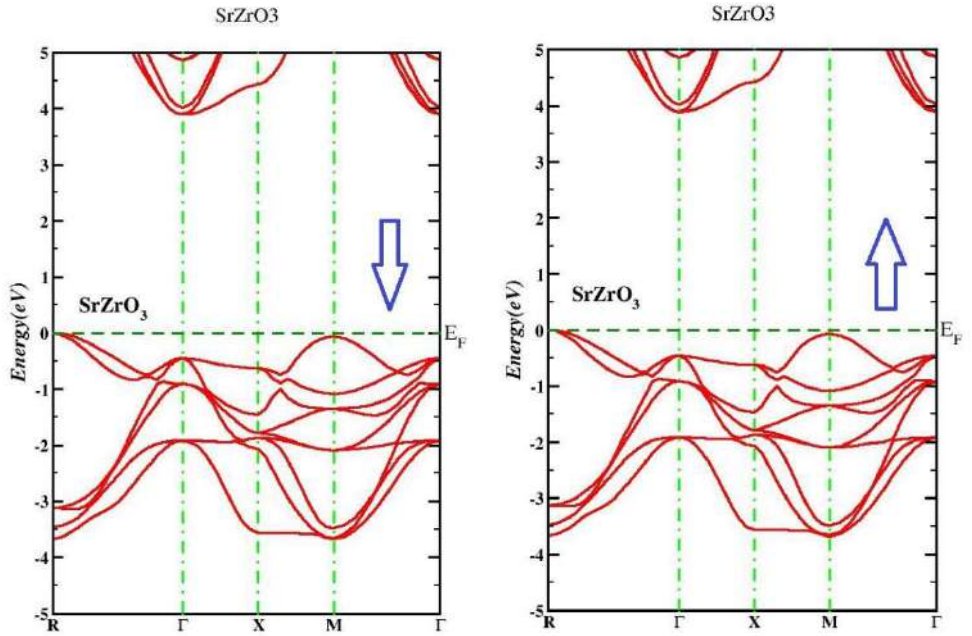

(e) (f)

Figure 13: (e) $SrZrO_3$ spin down and (f) $SrZrO_3$ spin up.

4.3 Total density of states (TDOS)

Calculated spectra of TDOS of $QZrO_3$ (Q = Br, Ca, Sr) is presented in Figure 14. We can observe from the spectra of TDOS that behavior of said compounds is same in majority and minority spins, (since we have no spin difference in our compounds that's why we have discussed only spin up) there is equal distribution of electron in majority and minority spin states. It result into zero net magnetic moment means that these compounds are non-magnetic in nature. We can also observe that different states are present at Fermi level that validates the fact established from the band constitutions that these compounds are semiconductor in nature. Spectra of TDOS are plotted for a continuous energy range of -6.0 to 6.0 eV by taking Fermi level at 0 eV.

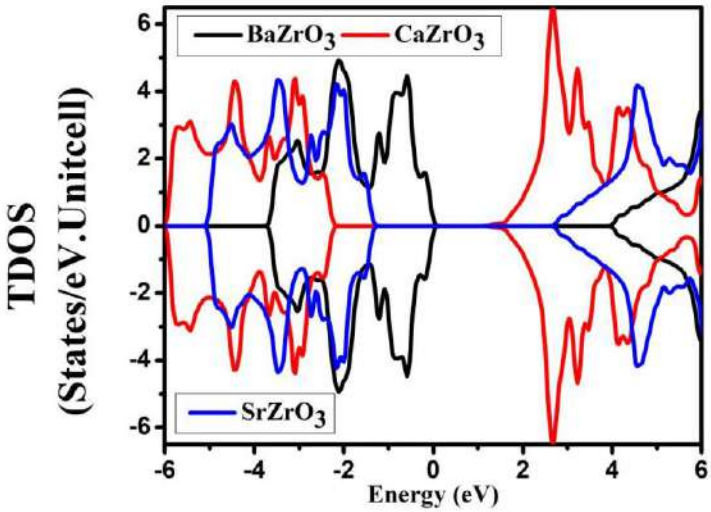

Figure 14: Total density of states of $QZrO_3$ (Q = Br, Ca, Sr).

4.4 Partial density of states (PDOS)

We can observe from the spectra or PDOS that $BaZrO_3$ compound have different behavior in valance and conduction band. Figure 15 shows spectra of $BaZrO_3$. This spectrum is plotted by using GGA approximation. In Figure 15 valance band is from -6.0 to 0 eV also valance band is divided into two major regions one is from -6.0 eV to -3.0 eV and second is from -3.0 eV to 0 eV. From Figure 4.6 we can calculate the contribution of sub shells of given compound from -6.0 to -3.0ev, in this region p-subshell of Ba has major contribution, d-subshell of Zr has major contribution and p-subshell of O has major contribution respectively.

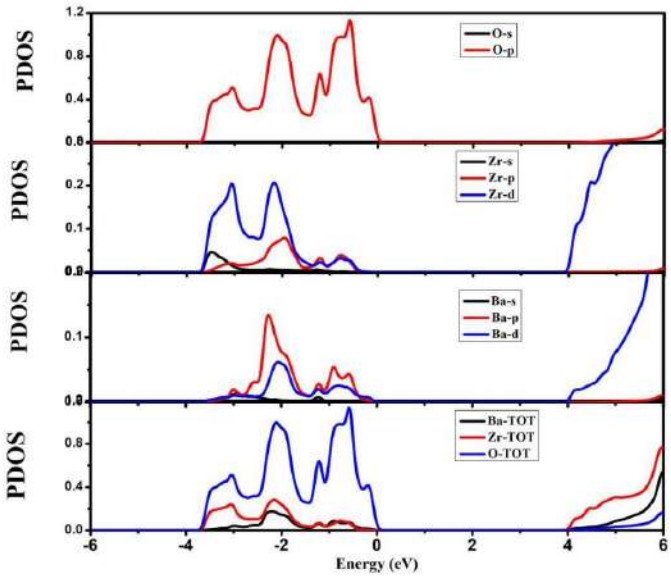

Figure 15: Total and partial density of states (TDOS and PDOS) for $BaZrO_3$.

Now we talk about Figure 16 which is spectra of $CaZrO_3$. This spectrum is plotted using GGA approximation. Since this approximation gives us the better results than GGA approximation. In Figure 16 valance band is from -6.0 to 0 eV also valance band is divided into two major regions one is from -6.0 eV to -3.0 eV and second is from -3.0 eV to 0 eV. From Figure 16 we can calculate the contribution of sub shells of given compound from -6.0 to -3.0ev, in this region p-subshell of Ca has minor contribution, d-subshell of Zr has major contribution and p-subshell of O has major contribution respectively.

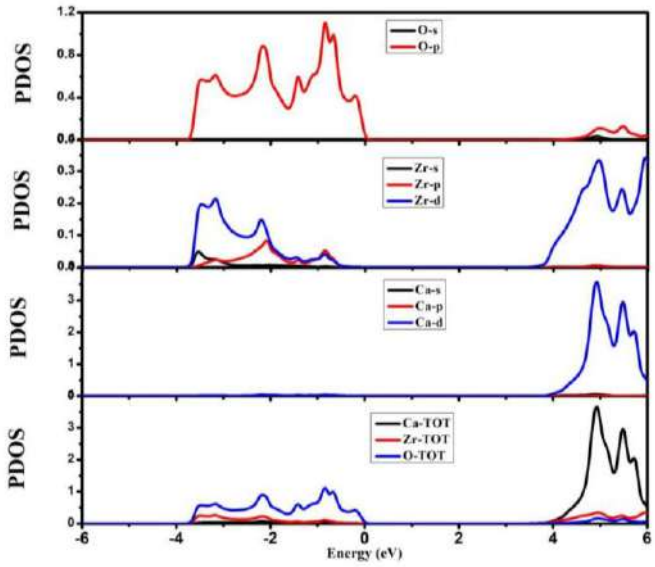

Figure 16: Total and partial density of states (TDOS and PDOS) for $CaZrO_3$.

In Figure 17 valance band is from -6.0 to 0 eV also valance band is divided into two major regions one is from -6.0 eV to -3.0 eV and second is from -3.0 eV to 0 eV. From Figure 17 we can calculate the contribution of sub shells of given compound from -6.0 to -3.0ev, in this region d-subshell of Sr has major contribution, d-subshell of Zr has major contribution and p-subshell of O has major contribution respectively. We can only plot the graph for majority spin as evident from TDOS the electronic behaviour is same in both spins. The Spectra shows that in the valance band the major contribution is provided by oxygen and minor contribution are made by p-subshell of Zr and s subshell of Sr, whereas in conduction band the major contributor is p-subshell of Zr and s subshell of Sr have minor contribution. Whereas in conduction band subshells of O have very minor impact. The PDOS confirms the insulator nature of material. The band gap is of 4.0 eV.

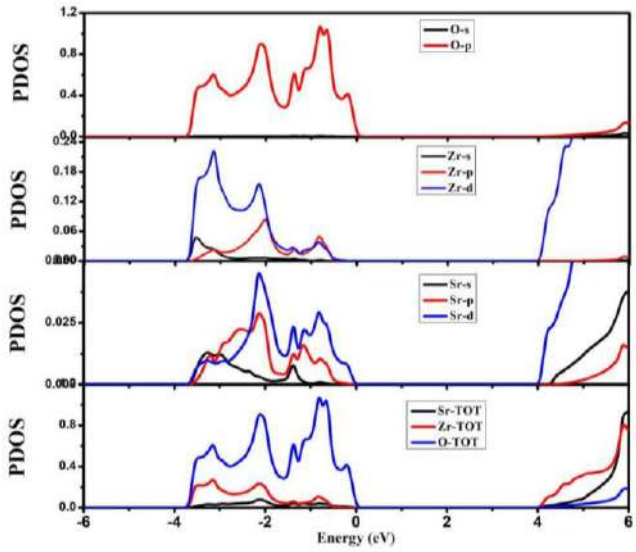

Figure 17: Total and partial density of states (TDOS and PDOS) for $SrZrO_3$.

4.5 Optical properties

a. Dielectric function:

Complete explanation of the optical properties of compounds under study can be provided by using real part $\varepsilon_1(\omega)$ and imaginary part & $\varepsilon_2(\omega)$ of complex dielectric function therefore, eligibility of $QZrO_3$ (Q = Br, Ca, Sr) can be judged by the knowledge of these properties Optical response of $QZrO_3$ (Q = Br, Ca, Sr) can be estimated by using the data of $\varepsilon_1(\omega)$ and $\varepsilon_2(\omega)$. Complex dielectric function(ω) consists of real part $\varepsilon_1(\omega)$ and imaginary par $\varepsilon_2(\omega)$. Frequency dependent complex dielectric function $\varepsilon(\omega)$ can be computed by using Eq. 3.3. Calculated spectra of imaginary part $\varepsilon_2(\omega)$ of complex dielectric function by using GGA approximation are illustrated in Figure 18 that are plotted for a continuous energy range of 0 to 14eV. We choose to show only the results obtained by using GGA approximation as these results are better as equated to the outcomes attained by using GGA approximation.

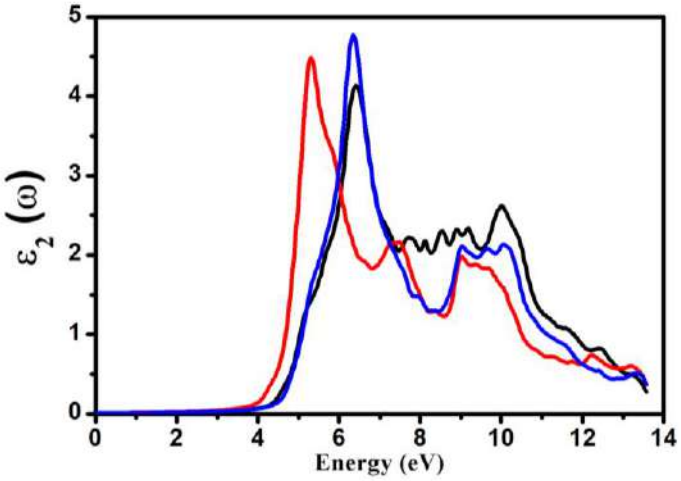

Figure 18: Imaginary part $\varepsilon_2(\omega)$of dielectric function of $QZrO_3$ (Q = Br, Ca, Sr).

Calculated spectra for $QZrO_3$ (Q = Br, Ca, Sr) are almost identical in shape however, slight optical anisotropy is present in these spectra that can be observed by the height and position of peaks.

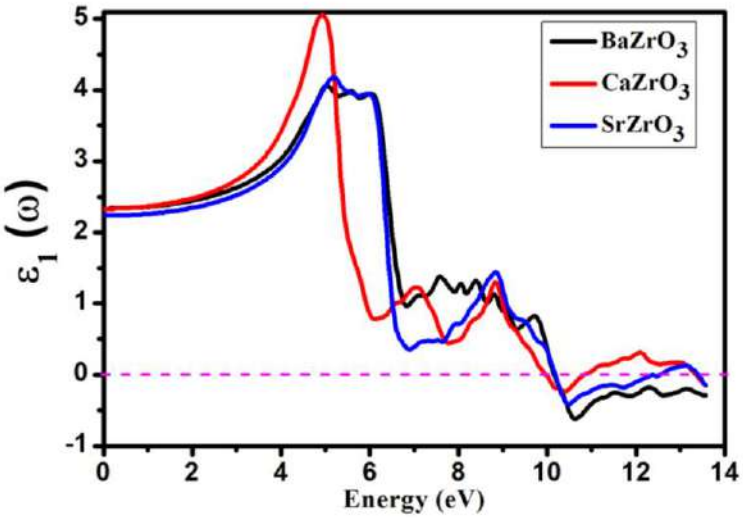

Figure 19: Real part $\varepsilon_1(\omega)$ of dielectric function of $QZrO_3$ (Q = Br, Ca, Sr).

Values of real part $\varepsilon_1(\omega)$ of complex dielectric function at zero frequency limit are known as static values of real dielectric function $\varepsilon_1(0)$, from spectra we can see that highest peaks for $BaZrO_3$ lies at 4.9 eV and peaks of $CaZrO_3$ lies at 5 eV and for $SrZrO_3$ lies at 5.2 eV respectively as shown in Figure 4.10. Static values for $BaZrO_3$ is 2.8, for $CaZrO_3$ is 2.7 and for $SrZrO_3$ is 2.55 respectively as shown in Figure 19. Frequency at which the graph enters in negative region is called Plasmon frequency. Spectra of $\varepsilon_1(\omega)$ becomes maximum at approximately 4.9 eV for $BaZrO_3$ respectively. And the minima refers to 10.6 eV, $\varepsilon_1(\omega)$tells us about the dispersion of incident photons. Rest of optical parameters such as refractive index, extinction coefficient, absorption coefficient, reflectivity, real optical conductivity and energy loss function can be calculated through utilizing designed values of real and imaginary parts of complex dielectric function.

b. Absorption Coefficient:

Frequency dependent absorption coefficient $\alpha(\omega)$ is calculated in order to get confirmation of former results that are obtained from dielectric function. Absorption coefficient$\alpha(\omega)$for $QZrO_3$ (Q = Br, Ca, Sr) can be calculated by using Eq. 4.6. Calculated spectra of absorption coefficient$\alpha(\omega)$by using GGA calculation are illustrated in Figure 20 that are plotted for a continuous energy range of 0 to 14 eV. Useful information regarding complete absorption of photons by the material when their energy in greater than energy band gap is provided by an optical limitation known as absorption coefficient.

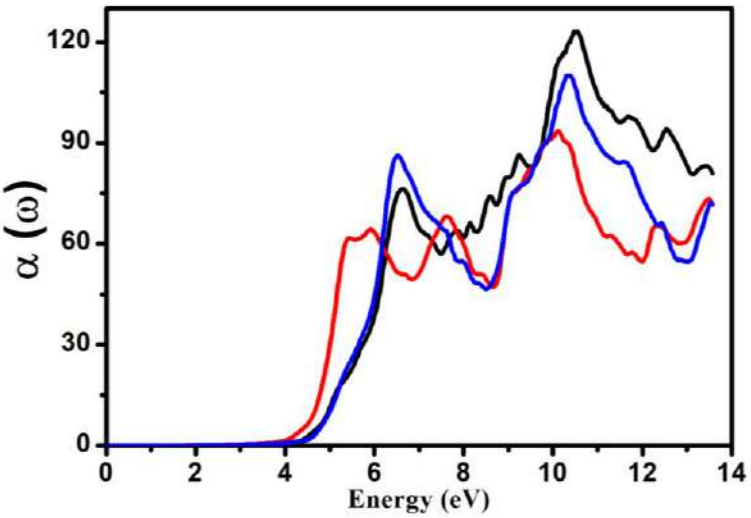

Figure 20: Absorption coefficient $\alpha(\omega)$ of $QZrO_3$ (Q = Br, Ca, Sr).

It is important to portray that maximum absorption of incident photons is present in lower ultraviolet (UV). This is an important property of the compounds that must be kept in mind for development of an efficient photo absorber devices. Calculated spectra of $\alpha(\omega)$shows noticeable anisotropy for the aforementioned compounds. Threshold values for $BaZrO_3$ lies at 3.8 eV and peaks of $CaZrO_3$ lies at 3.9 eV and for $SrZrO_3$ lies at 3.9 eV respectively as shown in Figure 20. Highest peaks in the spectra of $\alpha(\omega)$ for majority spin are present at approximately 10.5 eV for $BaZrO_3$, 10.1 eV for $CaZrO_3$ and 10.3 eV for $SrZrO_3$ respectively as shown in Figure 20.

c. Reflectivity Coefficient:

Values of reflectivity coefficient $R(\omega)$ at zero frequency limit are identified as static values of reflectivity coefficient (0). The static value for $BaZrO_3$ lies at 0.045 and peaks of $CaZrO_3$ lies at 0.048 and for $SrZrO_3$ lies at 0.04 respectively as shown in Figure 21 Anisotropy in the spectra of $R(\omega)$ for $BaZrO_3$, $CaZrO_3$ and $SrZrO_3$ are linked with electronic orbitals present in the compound. The highest peak occurs at 13.7 eV for $BaZrO_3$, 13.75 eV for $CaZrO_3$ and 13.8 eV for $SrZrO_3$ respectively as shown in Figure 21 And 45% dent photons will be reflected.

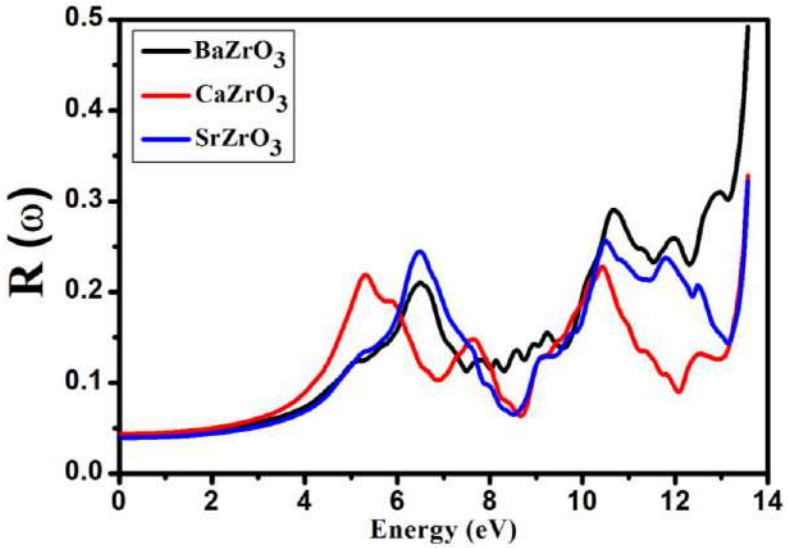

Figure 21: Reflectivity coefficient $R(\omega)$ of $QZrO_3$ (Q = Br, Ca, Sr).

d. Refractive Index

Refractive index $n(\omega)$is correspondent of the real part of complex dielectric function and it yield knowledge regarding dispersion of photons. Calculated spectra of $n(\omega)$ for $BaZrO_3$, $CaZrO_3$ and $SrZrO_3$. The spectra are almost identical in shape; however, slight optical anisotropy is present in these spectra that can be observed by the height and position of peaks. Values of $n(\omega)$at zero frequency limit are known as static values of (0), value for $BaZrO_3$ lies at 1.51, for $CaZrO_3$ lies at 1.52 and for $SrZrO_3$ lies at 1.5 respectively as shown in Figure 22. A good optical material has n between 1 and 2. The highest peak occur at 6.9 eV for $BaZrO_3$, 5,1 eV for $CaZrO_3$ and 6.8 eV for $SrZrO_3$ respectively as shown in Figure 22.

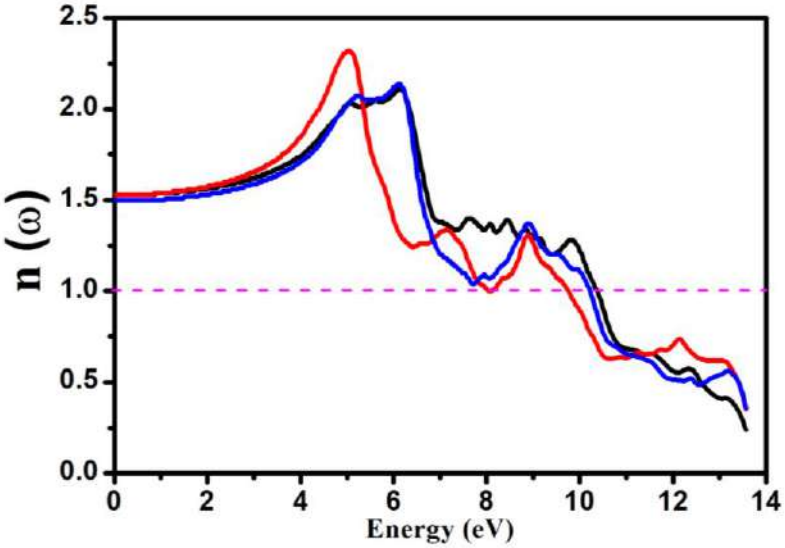

Figure 22: Refractive index $n(\omega)$ of $QZrO_3$ (Q = Br, Ca, Sr).

e. Extinction Coefficient

Calculated spectra of extinction coefficient $\mathbf{k}(\boldsymbol{\omega})$ shown in Figure 23. that are plotted for a continuous energy range of 0 to 14 eV.

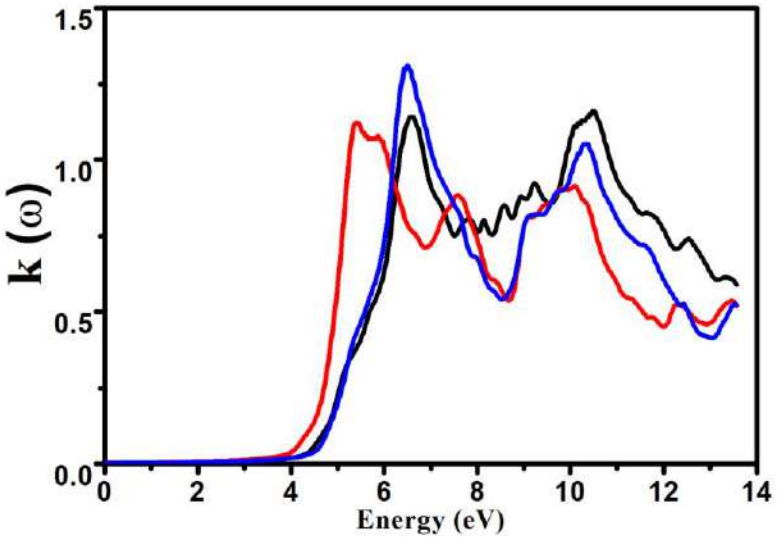

Figure 23: Extinction coefficient $\mathbf{k}(\boldsymbol{\omega})$ of $QZrO_3$ (Q = Br, Ca, Sr).

Extinction coefficient $\mathbf{k}(\boldsymbol{\omega})$ is correspondent of the imaginary part $\boldsymbol{\varepsilon_1(\omega)}$ of complex dielectric function and it gives knowledge about absorption of photons. Extinction coefficient $\mathbf{k}(\boldsymbol{\omega})$ for $QZrO_3$ (Q = Br, Ca, Sr) can be calculated by using Eq. 4.8.

Highest peaks in the spectra of $\mathbf{k}(\boldsymbol{\omega})$for majority spin are present at approximately at 10.9 eV for $BaZrO_3$, 4.8 eV for $CaZrO_3$ and 6.8 eV for $SrZrO_3$ respectively as shown in Figure 23. The spectra are almost identical in shape. However, slight optical anisotropy is present in these spectra that can be observed by the height and position of peaks. Threshold value start at 3.8 eV for $BaZrO_3$, 3.7 eV for $CaZrO_3$ and 3.9 eV for $SrZrO_3$ respectively as shown in Figure 23.

f. Optical Conductivity

Determined spectra of optical conductivity $\boldsymbol{\sigma(\omega)}$ for $QZrO_3$ (Q = Br, Ca, Sr) are shown in Figure 24 that are plotted for a continuous energy range of 0 to 14 eV.

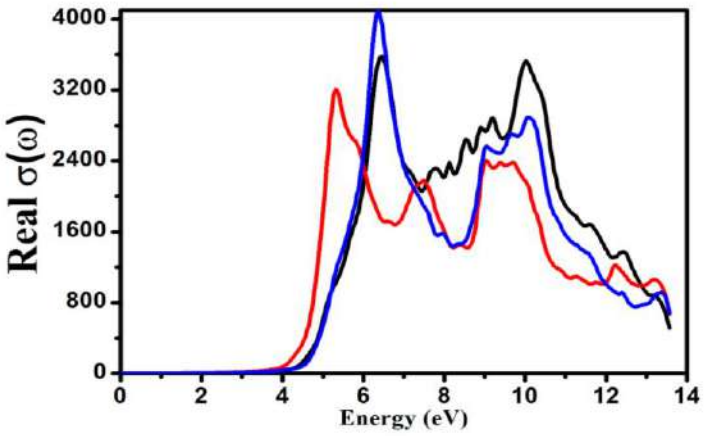

Figure 24: Optical conductivity real $\boldsymbol{\sigma(\omega)}$ of $QZrO_3$ (Q = Br, Ca, Sr).

Highest peaks in the spectra of $\sigma(\omega)$ for majority spin are present at approximately 6.9 eV for $BaZrO_3$, 4.9 eV for $CaZrO_3$ and 6.51 eV for $SrZrO_3$ respectively as shown in Figure 24. Threshold values for $BaZrO_3$ lies at 4 eV and peaks of $CaZrO_3$ lies at 3.7 eV and for $SrZrO_3$ lies at 3.9 eV respectively as shown in Figure 24.

g. Energy Loss Function

Energy loss function (ω) is worked to explain the loss of fast-moving electrons while passing within the medium. Computed spectra of energy loss function (ω) are shown in Figure 25 that are plotted for a continuous energy range of 0 to 14 eV.

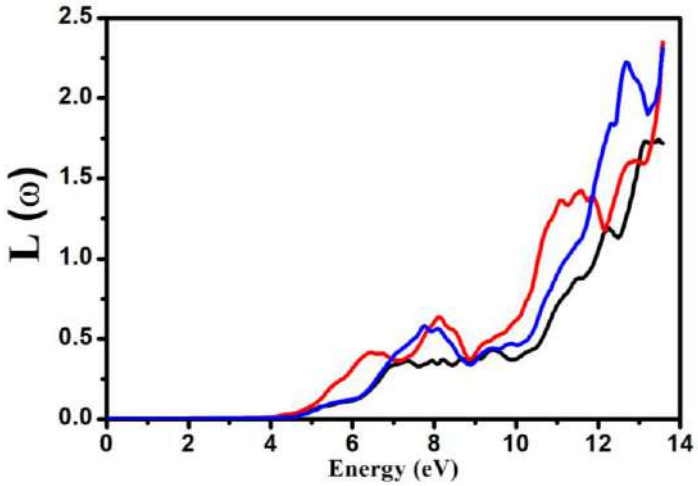

Figure 25: Energy loss function L(ω) of $QZrO_3$ (Q = Br, Ca, Sr).

Highest peaks in the spectra of (ω) for spin up are present from approximately 13.5 eV for $BaZrO_3$, 13.7 eV for $CaZrO_3$ and 13.69 eV for $SrZrO_3$ respectively as shown in Figure 25. Threshold values for $BaZrO_3$ lies at 4 eV and peaks of $CaZrO_3$ lies at 4.6 eV and for $SrZrO_3$ lies at 4.7 eV respectively as shown in Figure 25.

CONCULUSIONS

In conclusion, the FP–LAPW approach with the GGA (Generalized Gradient) approach was used in the Wien2k code to conduct a thorough investigation of the cubic phase of CaZrO3, SrZrO3, and BaZrO3. Furthermore, the cubic phases of CaZrO3 and SrZrO3 are high temperature structures, with the exception of BaZrO3. According to the study, CaZrO3 has some ductility, but SrZrO3 and BaZrO3 are brittle. These materials all exhibit large indirect band gaps. These zirconate perovskites exhibit greater optical absorption in the ultraviolet spectrum. Lastly, it is expected that this research will be useful in fine-tuning these materials' characteristics by changing the cation Q. The aforementioned materials' optical characteristics were also examined, and a plotted graph indicated that this material would be a good fit for optical devices because its refractive index is in the region of 2.045. The comprehensive potential calculation of the electrical and optical characteristics of QZrO3 (Q = Br, Ca, Sr) is done using the GGA approximation. We discover that these compounds exhibit substantial absorption in the energy spectrum between 4.0 eV and 12 eV. These materials are poor reflectors since they reflect 45% of the incident beam. The current work will give theorists and experimentalists reference data to practice these materials in the electronics sector.

REFERENCES:

[1] Adewale, A. A., Chik, A., & Zaki, R. M. (2020). Electronic properties of calcium and zirconium co-doped $BaTiO_3$. *Materials Science Forum, 1010*, 308–313. https://doi.org/10.4028/www.scientific.net/MSF.1010.308

[2] Alshoaibi, A. (2017). *Electrical properties of rare earth-doped barium titanate* (Doctoral dissertation, University of Sheffield).

[3] Brown, A., Müller, S., & Dobrotkova, Z. (2011). *Renewable energy: Markets and prospects by technology*. IEA Information Paper.

[4] Dahbi, S., Tahiri, N., El Bounagui, O., & Ez-Zahraouy, H. (2020). The new eco-friendly lead-free zirconate perovskites doped with chalcogens for solar cells: Ab initio calculations. *Optical Materials, 109*, 110444. https://doi.org/10.1016/j.optmat.2020.110444

[5] DeVries, R. C., & Burke, J. E. (1957). Microstructure of barium titanate ceramics. *Journal of the American Ceramic Society, 40*(6), 200–206. https://doi.org/10.1111/j.1151-2916.1957.tb12664.x

[6] Edri, E., Kirmayer, S., Mukhopadhyay, S., Gartsman, K., Hodes, G., & Cahen, D. (2014). Elucidating the charge carrier separation and working mechanism of $CH_3NH_3PbI_3$−xClx perovskite solar cells. *Nature Communications, 5*, 3461. https://doi.org/10.1038/ncomms4461

[7] Feng, L. M., Jiang, L. Q., Zhu, M., Liu, H. B., Zhou, X., & Li, C. H. (2008). Formability of ABO_3 cubic perovskites. *Journal of Physics and Chemistry of Solids, 69*(4), 967–974. https://doi.org/10.1016/j.jpcs.2007.10.063

[8] Gillani, S. S. A., Ahmad, R., Rizwan, M., Rafique, M., Ullah, G., Cao, C. B., & Jin, H. B. (2019). Effect of magnesium doping on band gap and optical properties of $SrZrO_3$ perovskite: A first-principles study. *Optik, 191*, 132–138. https://doi.org/10.1016/j.ijleo.2019.05.039

[9] Gillani, S. S. A., Ahmad, R., Zeba, I., Islah-u-din, Rizwan, M., Rafique, M., & Siddique, M. (2019). Structural stability of $SrZrO_3$ perovskite and improvement in electronic and optical properties by Ca and Ba doping for optoelectronic applications: A DFT approach. *Philosophical Magazine, 99*(24), 3133–3145. https://doi.org/10.1080/14786435.2019.1641957

[10] Green, M. A. (2015). Corrigendum to "Solar cell efficiency tables (version 46)." *Progress in Photovoltaics: Research and Applications, 23*(9), 1202. https://doi.org/10.1002/pip.2653

[11] Haertling, G. H. (1999). Ferroelectric ceramics: History and technology. *Journal of the American Ceramic Society, 82*(4), 797–818. https://doi.org/10.1111/j.1151-2916.1999.tb01840.x

[12] Hoat, D. M., Silva, J. R., & Blas, A. M. (2018). First-principles study of structural, electronic and optical properties of perovskites $CaZrO_3$ and $CaHfO_3$ in cubic phase. *Solid State Communications, 275*, 29–34. https://doi.org/10.1016/j.ssc.2018.02.016

[13] Im, J. H., Jang, I. H., Pellet, N., Grätzel, M., & Park, N. G. (2014). Growth of $CH_3NH_3PbI_3$ cuboids for high-efficiency perovskite solar cells. *Nature Nanotechnology, 9*(11), 927–932. https://doi.org/10.1038/nnano.2014.181

[14] Issa, M. A. A. (1992). Electrical properties of polycrystalline PTCR barium titanate. *Journal of Materials Science, 27*(13), 3685–3692. https://doi.org/10.1007/BF01151853

[15] Jonker, G. H. (1967). Halogen treatment of barium titanate semiconductors. *Materials Research Bulletin, 2*(4), 401–407. https://doi.org/10.1016/0025-5408(67)90050-6

[16] Kim, H. S., Lee, C. R., Im, J. H., Lee, K. B., Moehl, T., Marchioro, A., ... Park, N. G. (2012). Lead iodide perovskite sensitized all-solid-state submicron thin film mesoscopic solar cell with efficiency exceeding 9%. *Scientific Reports, 2*, 591. https://doi.org/10.1038/srep00591

[17] Kong, L. B., Zhang, T. S., Ma, J., & Boey, F. (2008). Progress in synthesis of ferroelectric ceramic materials via high-energy mechanochemical technique. *Progress in Materials Science, 53*(2), 207–322. https://doi.org/10.1016/j.pmatsci.2007.05.001

[18] Kuwabara, M., & Hamamoto, K. (2003). Electric field-induced birefringence in single grain boundaries of PTCR barium titanate ceramics above the Curie point. *Ferroelectrics, 290*(1), 71–81. https://doi.org/10.1080/00150190390216852

[19] Lamichhane, A., & Ravindra, N. M. (2021). First-principles study of cubic alkaline-earth metal zirconate perovskites. *Journal of Physics Communications, 5*(3), 035006. https://doi.org/10.1088/2399-6528/abeb41

[20] Lemanov, V. V., Sotnikov, A. V., Smirnova, E. P., Weihnacht, M., & Kunze, R. (1999). Perovskite $CaTiO_3$ as an incipient ferroelectric. *Solid State Communications, 110*(11), 611–614. https://doi.org/10.1016/S0038-1098(99)00152-1

[21] Lin, J. N., & Wu, T. B. (1990). Effects of isovalent substitutions on lattice softening and transition character of $BaTiO_3$ solid solutions. *Journal of Applied Physics, 68*(3), 985–993. https://doi.org/10.1063/1.347181

[22] Liu, D., & Kelly, T. L. (2014). Perovskite solar cells with a planar heterojunction structure prepared using room-temperature solution processing techniques. *Nature Photonics, 8*(2), 133–138. https://doi.org/10.1038/nphoton.2013.342

[23] Meena, S. K., Dashora, A., Heda, N. L., & Ahuja, B. L. (2019). Compton spectroscopy and electronic structure study for tetragonal barium titanate. *Radiation Physics and Chemistry, 158*, 46–52. https://doi.org/10.1016/j.radphyschem.2019.01.021

[24] Mitchell, R. H. (2002). *Perovskites: Modern and ancient* (Vol. 7). Almaz Press.

[25] Nazir, G., Ahmad, A., Khan, M. F., & Tariq, S. (2015). Putting DFT to the trial: First-principles pressure-dependent analysis on optical properties of cubic perovskite $SrZrO_3$. *Computational Condensed Matter, 4*, 32–39. https://doi.org/10.1016/j.cocom.2015.04.003

[26] Pazos-Outón, L. M., Szumilo, M., Lamboll, R., Richter, J. M., Crespo-Quesada, M., Abdi-Jalebi, M., ... Deschler, F. (2016). Photon recycling in lead iodide perovskite solar cells. *Science, 351*(6280), 1430–1433. https://doi.org/10.1126/science.aaf1168

[27] Rodríguez, J. I., Ayers, P. W., Götz, A. W., & Castillo-Alvarado, F. D. L. (2009). Virial theorem in the Kohn–Sham density-functional theory formalism. *The Journal of Chemical Physics, 131*(2), 021101. https://doi.org/10.1063/1.3154504

[28] Rizwan, M., Aleena, S., Shakil, M., Mahmood, T., Zafar, A. A., Hussain, T., & Farooq, M. H. (2020). A computational insight of electronic and optical properties of Cd-doped $BaZrO_3$. *Chinese Journal of Physics, 66*, 318–326. https://doi.org/10.1016/j.cjph.2020.05.010

[29] Rizwan, M., Anam, S., Farman, M., Akgul, A., & Uzma, M. (2020). Role of Zn in modification of electronic and optical properties of c-$SrZrO_3$: A computational insight. *Physica Scripta, 95*(8), 085212. https://doi.org/10.1088/1402-4896/ab9b5a

[30] Tahiri, O., Kassou, S., & Mrabet, R. (2018). First principles calculations of electronic and optical properties for mixed perovskites: $Ba_{1-x}Ca_xTiO_3$ and $Ba_{1-x}Sr_xTiO_3$ (x = 0.4, 0.6). *Materials and Devices, 3*, 2004–2018.

[31] Woodward, P. M. (1997). Octahedral tilting in perovskites. I. Geometrical considerations. *Acta Crystallographica Section B, 53*(1), 32–43. https://doi.org/10.1107/S0108768196010710

[32] Zeba, I., Jabeen, R., Ahmad, R., Shakil, M., Rafique, M., Rizwan, M., & Gillani, S. S. A. (2020). Effect of anomalous behavior of Be-doping on structural stability, bandgap and optical properties in comparison with Mg-doped $BaZrO_3$ perovskite. *Optical and Quantum Electronics, 52*(5), 1–14. https://doi.org/10.1007/s11082-020-02320-0

[33] Zeba, I., Ramzan, M., Ahmad, R., Shakil, M., Rizwan, M., Rafique, M., & Gillani, S. S. A. (2020). First-principles computation of magnesium doped $CaZrO_3$ perovskite. *Solid State Communications, 313*, 113907. https://doi.org/10.1016/j.ssc.2020.113907